2020-08-30

# Supercapacitors with lithium-ion electrolyte: An experimental study and design of the activated carbon electrodes via modelling and simulations

Markoulidis, F



10.1016/j.carbon.2020.04.017
Carbon
Elsevier BV

# Supercapacitors with lithium-ion electrolyte: an experimental study and design of the activated carbon electrodes via modelling and simulations

*Foivos Markoulidis[1,2], Josh Bates[1], Constantina Lekakou[1*], Robert Slade[2], Giuliano M. Laudone[3]*

[1]Centre for Engineering Materials, Department of Mechanical Engineering Sciences, Faculty of Engineering and Physical Sciences, University of Surrey, UK

[2] Chemistry Department, Faculty of Engineering and Physical Sciences, University of Surrey, UK

[3] Faculty of Science and Engineering, University of Plymouth, UK

[*]Corresponding author, email: c.lekakou@surrey.ac.uk

**ABSTRACT**

Electrochemical double layer capacitors (EDLCs) are investigated with activated carbon electrodes and a lithium-ion electrolyte, in anticipation of potential future applications in hybridised battery-supercapacitor devices and lithium ion capacitors. An experimental study of a symmetric electrochemical double layer capacitor (EDLC) with activated carbon (AC) electrodes on aluminium foil current collectors and electrolyte 1 M $LiPF_6$ in EC:EMC 50:50 v/v concludes a stability window to a maximum potential of 3 V, an equivalent in series resistance of 48 ohm for 1 $cm^2$ cell area (including the contact resistance between electrode and current collector) and an average specific electrode capacitance of 50.5 F $g^{-1}$. Three AC electrode materials are assessed via computer simulations based on a continuum ion and charge transport model with volume-averaged equations, considering the pore size distribution for each electrode material and, depending on pore size, transport of tetrahedral solvated or flat solvated $Li^+$ ions and solvated or desolvated $PF_6^-$ ions. The computer simulations demonstrate that the best electrode material is an AC coating electrode with a hierarchical pore size distribution measured in the range of 0.5-180 nm and bimodal shape, and specific surface area BET = 808 $m^2$ $g^{-1}$.

## 1. INTRODUCTION

Following the concept of application-specific composite supercapacitors [1] which include hybridised electrodes of high power and high energy materials of optimised composition, depending upon the energy-to-power requirement of the specific application, sharing the same electrolyte in the same device, research has extended to hybrid battery-supercapacitor devices [2] where the battery component would provide the high specific energy and the supercapacitor component would provide the high specific power. As such, the battery and supercapacitor electrodes will share the same electrolyte, most probably a lithium-ion electrolyte required for the common lithium-ion batteries. Hence, a lithium-ion electrolyte is the focus of this study with the view of applications in hybrid battery-supercapacitor devices, hybridised at electrode level and sharing the same electrolyte as we have shown for electrodes of different power and energy density in our previous study of a novel application-specific composite supercapacitor [1]. The present study is concerned with the optimisation of the pore size distribution of the electrodes of the supercacapacitor part of a hybrid lithium-ion battery-supercapacitor device, to maximise ion transport of a lithium-ion electrolyte and resulting capacitance upon charge.

Common supercapacitors are electrochemical double layer capacitors (EDLCs) with high surface area electrode materials [3-6] such as activated carbon (AC) and graphene, also containing conductive additives such as carbon black and multiwall carbon nanotubes [7-8]. Given the low voltage limit of 1.1 V of aqueous electrolytes in symmetric EDLCs [9], organic electrolytes such as $TEABF_4$ in acetonitrile or propylene carbonate (PC) [1-8] are commonly employed for EDLCs cycled to a maximum operating voltage of 2.7 V. Over many years of research and development, such electrolytes have been optimised in terms of their ion size and solvated ion size to fit in the pore size distribution of electrode materials, verified in early experimental and theoretical studies

[10-11]. Furthermore, a recent model of ion transport using volume-averaged equations at continuum and taking into account the pore size distribution at every point in the electrodes and simulations employing electrolytes 1M $TEABF_4$ in acetonitrile or PC [12] demonstrated the importance of fast transport of solvated ions in large macro- and meso-channels, also providing high power, as well as the importance of small, high surface area micropores, accessible by the desolvated ions, in providing high capacitance and large stored energy. Another advantage of these organic electrolytes is their lower viscosity than ionic liquid electrolytes [13] and gel electrolytes such as $LiClO_4$ in polyvinyl alcohol [14]. Furthermore, supercapacitor recycling protocols [15] have been established for EDLCs with carbonaceous electrodes and organic liquid electrolytes, including dissolution of binder [16-17] and separation of carbonaceous electrode materials via dielectrophoresis [18].

There is a lack of data for EDLCs with lithium-ion electrolytes that are necessary in hybridized lithium-ion battery-supercapacitor devices and lithium-ion capacitors. Looking into lithium-ion capacitors, the stability of activated carbon electrodes was studied in $LiPF_6$/PC and $LiPF_6$/EC:DMC electrolytes and compared with that in $TEABF_4$/acetonitrile electrolyte [19]: it was found that $LiPF_6$/EC:DMC yielded 4.5 times higher device resistance than $TEABF_4$/acetonitrile and that the electrodes were stable in the range of 1.6-4.4 V for $LiPF_6$/EC:DMC and 1.3-4.4 V $LiPF_6$/PC. Apart from this paper, no detailed study has been carried out for lithium-ion electrolytes to evaluate the effect of the solvated ion size on ion transport and accessibility of pores in porous electrodes. It is clear that, if lithium-ion electrolytes are to be employed in supercapacitors, lithium-ion capacitors and hybridised battery-supercapacitor devices, the pore size distribution of the porous carbonaceous electrodes for the capacitor function needs to be optimized for these electrolytes.

$Li^+$ ion transport in batteries is generally considered in terms of diffusion of desolvated ions [20] given the dense microstructure of battery electrodes. Newman's model considers a macropore-scale continuum for the inter-particle voids, where the Poisson–Nernst–Planck equations are applied, and a $Li^+$ ion diffusion model for the solid particles material in which the ions are transported via diffusion through the solid phase of the particles [21]. Biesheuvel et al [22] modelled ion transport in supercapacitors, considering homogeneous-sized pores and applying the Poisson–Nernst–Planck equations for the transport of desolvated ions while charge was stored in the Stern layer. This has been extended by our team [12] to a model for ion transport at continuum level across the supercapacitor materials, taking into account a discrete pore size distribution.

The present investigation starts with an experimental study of a typical AC-coating based EDLC with electrolyte 1 M $LiPF_6$ in EC:EMC 50:50 v/v. This electrolyte has been selected as a common electrolyte in lithium-ion batteries, such as $LiFePO_4$ batteries, which may be employed in envisaged future research of our team in hybridized battery-supercapacitor devices. Coin cells are fabricated and tested in electrochemical impedance spectroscopy (EIS), cyclic voltammetry (CV) to different maximum voltage values, and galvanostatic charge-discharge (GCD) at different rates. A novel continuum level model is presented of volume-averaged equations of ion and charge transport across the electrodes, with the novel model features of (a) taking into account the full pore size distribution and (b) considering solvated and desolvated ions depending on the ion and pore size. Simulations of the GCD tests follow for the experimental case- study and the predictions are compared with the experimental data. Further parametric studies are based on simulations for two more case-studies with the same electrolyte but different pore size distribution electrodes to assess the effect of the pore size and pore size distribution in supercapacitors with Li-ion

electrolyte and offer new insights about the design of the corresponding activated carbon electrodes.

## 2. CONTINUUM, VOLUME-AVERAGED ION AND CHARGE TRANSPORT MODEL

Volume-averaged continuum equations [12, 23-26] are presented for one-dimensional ion and charge transport through the EDLC cell thickness, in the x-direction, as shown in the schematic in Fig.1. A discrete pore size distribution of pore sizes p = 1 to $N_p$, is considered at each x-position of each electrode and parallel volume-averaged continuum ion transport equations are solved for each pore size larger than the desolvated ion size:

$$\frac{\partial \varepsilon_p \alpha_{i,p}}{\partial t} - \frac{\partial}{\partial x}\left(\frac{z_i F D_{i,p} \alpha_{i,p} F_{decay,i}}{RT}\frac{\partial \phi_2}{\partial x}\right) = \frac{\partial}{\partial x}\left(\varepsilon_p D_{i,p} F_{decay,i}\ \frac{\partial \alpha_{i,p}}{\partial x}\right) + \frac{I_{i,p-1/p} - I_{i,p/p+1}}{\Delta x} \qquad (1)$$

Transient term; drift current term; diffusion term; inter-pore current fluxes

where $\alpha_{i,p}$ is the volume fraction of ion i ($^+$ or $^-$ ions) in pore size p, given as a function of the respective ion concentration in pore size p, $c_{i,p}$, by the equation:

$$\alpha_{i,p} = c_{i,p} N_A V_i \qquad (2)$$

$\varepsilon_p$ is the volume fraction of pore sized p, t is time, $z_i$ is the number of transferred electrons for ion i, F is the Faraday constant, R is the ideal gas constant, T is the absolute temperature, $D_{i,p}$ is the diffusion coefficient of ion i in pore p (solvated or desolvated ion, depending on pore size), $\phi_2$ is the potential of electrolyte phase in the non-Stern region, $N_A$ is the Avocadro's number and $V_i$ is the volume of ion i.

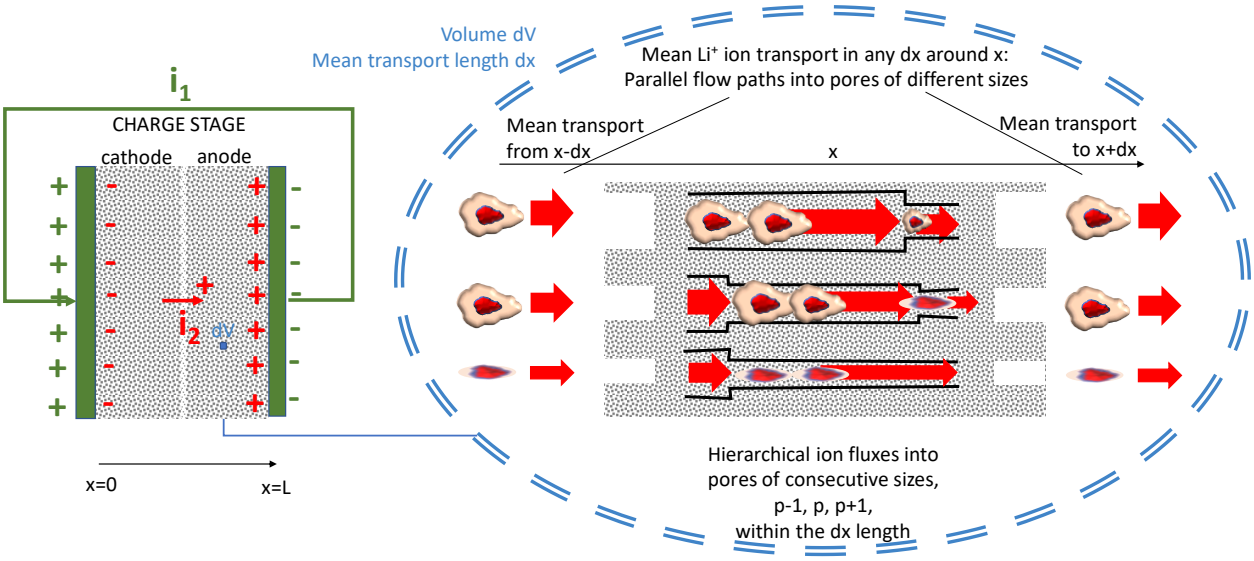


**Fig.1** Schematic for the continuum ion transport model. (a) EDLC cell, charges and currents during charge (b) phenomenological continuum $Li^+$ ion transport model at any x position in the electrode depicting tetrahedral solvated $Li^+$ ions in macro-, meso- and large micropores and flat solvated $Li^+$ ions in small slit micropores

Given the results of the molecular modelling of the solvated cation $Li^+$ in a small micro-slit pore between two graphene sheets originally at a distance of 0.56 nm in section 5.1, which yielded a flat solvated $Li^+_{EC:EMC}$ with a coordination number of 4, the easy desolvation of $PF_6^-{}_{EC:EMC}$ to $PF_6^-$ (Table SI-1), and also the PSD distribution measurements available to a minimum of 0.5 nm in section 4.1, the following assumptions have been made in the model for the electrolyte of this study 1M $LiPF_6$ in EC:EMC:

(a) For $d_p \geq d_{Li+/EC:EMC}$, the cation is transported in the form of a tetrahedral solvated ion of size $d_{Li+/EC:EMC}$, as given in Table SI-1.

For 0.5 nm < $d_p$ < $d_{Li+/EC:EMC}$, the cation is transported in the form of a flat solvated ion of size $d_{Li+}$, as given in Table SI-1, determined by molecular modelling presented in section 4.1.

(b) For $d_p \geq d_{PF6-/EC:EMC}$, the anion is transported in the form of a solvated ion of size $d_{PF6-/EC:EMC}$, as given in Table SI-1.

For 0.5 nm < $d_p$ < $d_{PF6-/EC:EMC}$, the anion is transported in the form of a desolvated ion of size $d_{PF6}$ = 0.5 nm, as given in Table SI-1.

However, for pores smaller than the solvated ion size, ion desolvation and entering the micropore pore during charge might take some time until the ions have sufficient electrochemical energy, $E_{EC}$, accumulated from charging to overcome the desolvation energy barrier. For this reason, a decay factor, $F_{decay,i}$, is applied to the drift current, diffusion and inter-pore current flux terms in equation (1) for each ion i, such that:

For $d_p \geq d_{solv.ion,i}$: $F_{decay,i} = 1$ (no desolvation to take place, ion is solvated)

For $d_p < d_{solv.ion,i}$: $$F_{decay,i} = e^{-\left(\frac{\Delta E_i}{RT+E_{EC}}\right)} \quad (3)$$

with the desolvation energy, $\Delta E_i$, given by the relation [27]:

$$\Delta E_{i,p} = E_i \Delta n_i / n_i \quad (4)$$

where $E_i$ is the solvation energy for the first solvent shell around ion i, $n_i$ is the coordination number of ion i and $\Delta n_i$ is the change of coordination number in desolvation of ion i in a small micropore. The desolvation energy barrier is assumed to be encountered only when ions enter small

micropores, not when they leave them and enter larger pores in which case they may become solvated but assumingly without having to overcome any energy barrier for solvation.

The ion transport equation (1) includes inter-pore fluxes (Fig.1) between pores of consecutive sizes, $d_{p-1}$, $d_p$ and $d_{p+1}$: $I_{i,p-1/p}$ from pore p-1 to pore size p, and $I_{i,p/p+1}$ from pore p to pore p+1, given by the general relation:

$$I_{i,p-1/p} = F_{decay,i} \frac{\varepsilon_{p-1} d_p^2}{\varepsilon_p d_{p-1}^2} \frac{z_i N_A V_i t_{i,p} i_2}{F} \quad (5)$$

where $i_2$ is the ion current density in the electrolyte phase and $t_{i,p}$ is the transference number of ion i in pore size p. Similarly to the drift current term in equation (1), the inter-pore current flux difference, $I_{i,p-1/p} - I_{i,p/p+1}$, is applied over a characteristic length which has been assumed in equation (1) to be of the same magnitude as dx.

The diffusion coefficient, $D_{i,p}$, is given by the following relation [28, 29]:

$$D_{i,p} = \frac{\varepsilon_p^{1.5} \delta k_B T}{2\pi\eta(d_{solv.ion,i} \text{ or } d_{ion,i})} \quad (6)$$

where $k_B$ is the Boltzmann's constant. $D_{i,p}$ depends on the ion size, solvated ion size $d_{solv.ion,i}$ or desolvated ion size $d_{ion,i}$, depending on the pore size, and takes into account the tortuosity of the porous medium via the term $\varepsilon_p^{1.5}$ [28], and the pore constrictivity against the ion via the constrictivity factor, $\delta$, given by the relation [30]:

$$\delta_{i,p} = \left(1 - \frac{d_{solv.ion,i} \text{ or } d_{ion,i}}{d_p}\right)^4 \quad (7)$$

The viscosity $\eta$ of the electrolyte solution is given by the following relation, as a function of the solvent viscosity, $\eta_o$, and the ion volume fractions [12]:

$$\eta = \eta_o \frac{[1+0.5(\alpha_{+,p}+\alpha_{-,p})]^{4.5}}{[1-(\alpha_{+,p}+\alpha_{-,p})]^2} \quad (8)$$

The ion current density in each pore size p at each x-position in electrodes is given by:

$$i_{2,p} = -\sigma_{2,p}\frac{\partial \phi_2}{\partial x} - \frac{\sigma_{2,p}RT}{F}\left[t_{+,p}\frac{\partial lnc_{+,p}}{\partial x} - t_{-,p}\frac{\partial lnc_{-,p}}{\partial x}\right] \quad (9)$$

where $\sigma_{2,p}$ is the electrolyte conductivity in pore p given by the Nernst-Einstein equation [31]:

$$\sigma_{2,p} = \frac{F^2[(z_+)^2 D_{+,p}c_{+,p} + (z_-)^2 D_{-,p}c_{-,p})}{RT} \quad (10)$$

The current density in the electrolyte phase at each position x is then calculated by:

$$i_2 = \sum_{p=1}^{N_p} \varepsilon_p i_{2,p} \quad (11)$$

whereas the current density in the solid phase, $i_1$, is given by:

$$i_1 = -\sigma_1 \frac{\partial \phi_1}{\partial x} \tag{12}$$

where $\sigma_1$ is the electrical conductivity of the solid phase and $\phi_1$ is the potential of solid phase. The charge conservation equation is expressed by:

$$\frac{\partial i_1}{\partial x} + \frac{\partial i_2}{\partial x} = 0 \tag{13}$$

Further to the bulk electrolyte potential $\phi_2$, the potential difference across the Stern layer (of thickness of one desolvated ion in this study: $L_{stern} = d_{ion}$) is given by the relation [22]:

$$\Delta\phi_{stern,i,p} = \frac{c_{i,p} z_i F v_p L_{stern}}{A_p \varepsilon_o \varepsilon_r} \tag{14}$$

where $A_p$ is the specific wall surface area of pore, $v_p$ is the specific pore volume, $\varepsilon_o$ is the vacuum permittivity and $\varepsilon_r$ is the dielectric constant of electrolyte.

The system of the above equations was discretised and solved using the implicit finite difference/finite volume method [23, 26, 32]. The initial condition is that in neutral state, all pores greater than the larger desolvated ion are filled with electrolyte, so that $c_{i,p} = k_d c_o$, where $k_d$ is the dissociation constant of the electrolyte. When charging starts, each type of ion is headed towards the corresponding counter-electrode.

## 3. EXPERIMENTAL PART

### 3.1 Materials

Three electrodes were prepared and all three were characterised in terms of their pore size distribution, so that they may be used in the parametric simulation studies. EDLC cells were fabricated and tested experimentally only with *Electrode 1*.

*Electrode 1*: a coating was manufactured on aluminium foil (Goodfellow) as current collector. The coating consisted of 90 wt% AC powder, peat bog-derived charcoal (Sigma Aldrich: 4C Norit A charcoal, specific surface area BET = 1000 $m^2g^{-1}$, particle size: 10–15% greater than 74 μm and 70–75% greater than 10 μm), 5 wt% acetylene carbon black (Alfa Aesar; average particle size 42 nm, specific surface area, BET =75 $m^2g^{-1}$, bulk density 170–230 $kgm^3$) and 5 wt% PVDF (Sigma Aldrich: MW=534000).

*Electrode 2*: a coating was manufactured on aluminium foil (Goodfellow) as current collector. The coating consisted of 90 wt% AC TE320 with approximately 30% activation (MAST Carbon), 5 wt% acetylene carbon black (Alfa Aesar; average particle size 42 nm, specific surface area, BET =75 $m^2g^{-1}$, bulk density 170–230 $kgm^3$) and 5 wt% PVDF (Sigma Aldrich: MW=534000).

*Electrode 3:* phenolic-derived AC Kynol fabric ACC-507-15 (Kynol Europe Gmbh: BET = 1461 $m^2g^{-1}$).

The coatings were manufactured from a slurry of the solid materials in a PVDF solution in N-Methyl-2-pyrrolidone (NMP) via the doctor blade technique. The coatings were then dried in an oven at 120 °C for 4 h.

Electrolyte was 1 M $LiPF_6$ in EC:EMC 50:50 v/v (Sigma Aldrich). An assembly of Celgard 3501/glass fibre filter GF/F/Celgard 3501 was used as separator in the EDLC coin cells.

### 3.2 EDLC Fabrication

Symmetric EDLC coin cells (2032 size of coin case) were fabricated, with all the assembly and fabrication taking place in an argon filled glovebox with moisture and oxygen content below 10 ppm. The EDLC coin cells were symmetric EDLCs, with electrode discs of 15 mm diameter. The electrode was AC coating *Electrode 1* of 90 μm thickness and areal density of 4.6 mg $cm^{-2}$. Electrolyte was 1 M $LiPF_6$ in EC:EMC 50:50 v/v.

### 3.3 Material characterisation and EDLC testing

All three electrodes were also characterised in nitrogen adsorption/desorption experiments, using a BELSORP-Max at the University of Plymouth. The pore size distribution was determined from the adsorption/desorption isotherms through GCMC (Grand Canonical Monte Carlo) simulations, assuming a slit pore shape. The electrodes were also characterised under a high-resolution scanning electron microscope HR-SEM JEOL-7100F and an atomic force microscope (AFM), a Bruker Dimension Edge AFM Instrument, in tapping mode, at the University of Surrey.

The EDLC coin cells were tested using a GAMRY 1000 potentiostat at the University of Surrey. The cells were subjected to (a) electrochemical impedance spectroscopy (EIS) in the frequency range of 10 mHz-1 MHz; (b) cyclic voltammetry (CV) to increasingly higher maximum voltage to evaluate electrode materials stability in the Li-ion electrolyte: CV tests were carried out to maximum voltage of 0.5, 1, 1.5, 2, 2.5, 3 and 3.6 V and for each maximum voltage value CV tests

were performed at different rates: 1, 2, 5, 10, 50 and 100 mV $s^{-1}$, three cycles at each rate; (c) galvanostatic charge-discharge (GCD) at different constant current values.

## 4. EXPERIMENTAL RESULTS

### 4.1 Electrode material characterization

Fig.2 displays the experimental data of the pore size distributions (PSDs) for each of the three electrodes and the caption contains the derived specific surface areas. *Electrode 1* (AC-based coating) has a bimodal pore size distribution with a main peak at 0.635 nm and a smaller peak at 1.41 nm. *Electrode 3* (phenolic-derived AC Kynol fibres) has also a bimodal pore size distribution with a main peak at 0.635 nm and a smaller peak at 1.31 nm but both peaks are higher than for *Electrode 1* and, as a result, *Electrode 3* has the largest specific surface area. *Electrode 2* (phenolic-derived AC-based coating) has one broad peak at 1.3 nm, spanning from 0.5 to 3.5 nm and relatively large specific surface area.

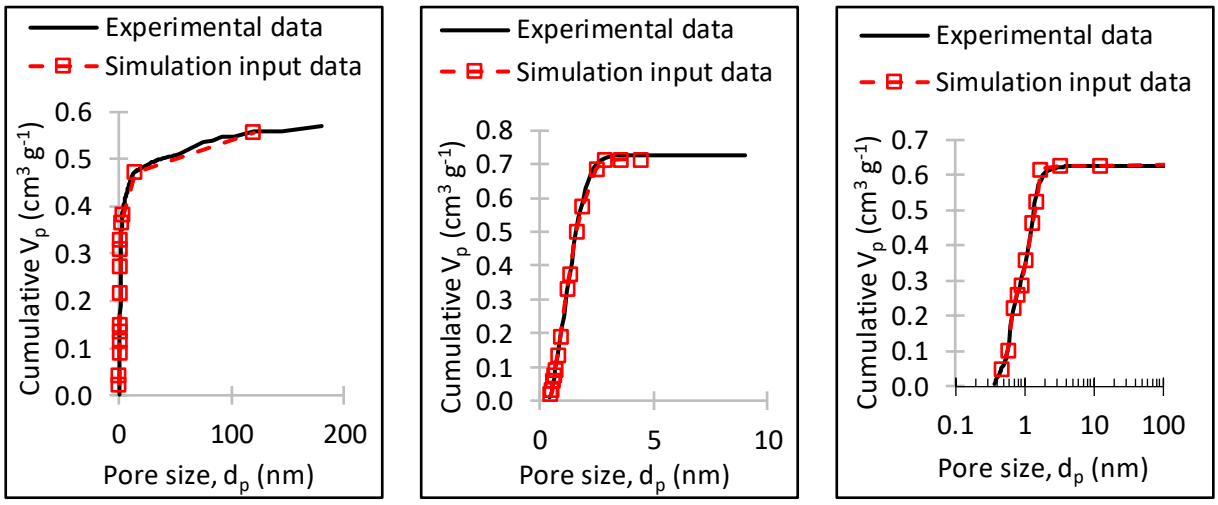

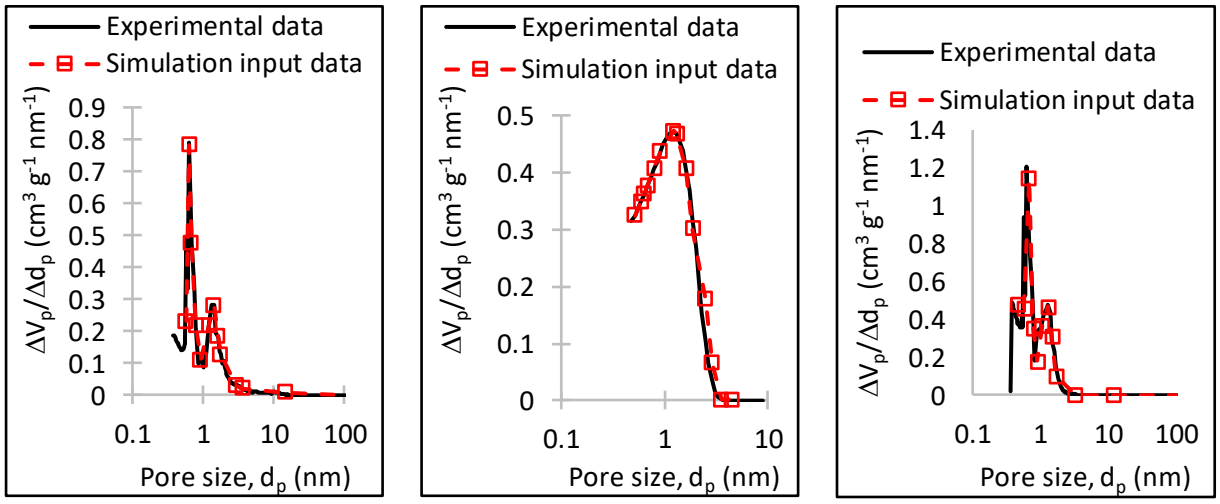


*Electrode 1* *Electrode 2* *Electrode 3*

**Fig.2** Pore size distribution (PSD) of each of the three electrodes and fitted discrete PSD lines used as input data in the simulations for the three case-studies. Assuming slit shape pores, processing of the experimental data yields the cumulative surface area for each electrode as follows: *Electrode 1*: 808.3 $m^2$ $g^{-1}$, *Electrode 2*: 1273.7 $m^2$ $g^{-1}$, *Electrode 3*: 1491 $m^2$ $g^{-1}$.

Discrete PSDs were fitted to the experimental lines, in order to use these discrete PSDs as input data for the simulations using the continuum model described in section 2. The fitted discrete PSDs consisted of 14, 15 and 12 pore sizes for *Electrode 1*, *Electrode 2* and *Electrode 3*, respectively.

Fig.3 presents examples of SEM and AFM images for the three electrodes illustrating their microstructure at macropore scale. Large cylindrical macropores can be seen in all electrodes in the SEM images. AFM images display cylindrical macropores of 50-100 nm in *Electrode 1* and of 15-50 nm in *Electrode 3*; in contrast, slit pores of 10-20 nm can be seen in *Electrode 2*. Due to limitations in the resolution of the SEM and AFM instruments, micropores cannot be seen although they clearly dominate the PSD data in Fig.2.

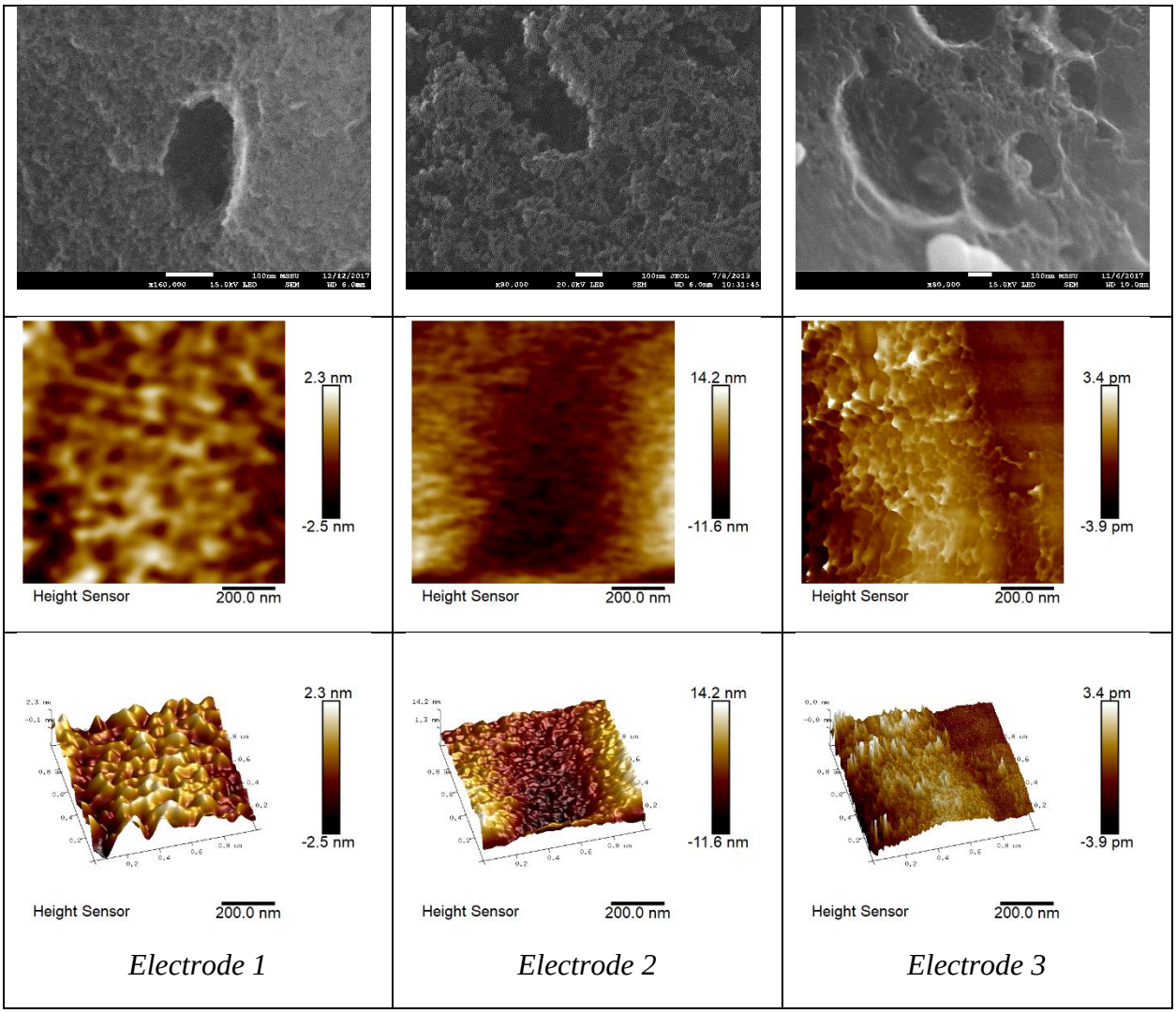


**Fig.3** SEM images (top row) and AFM images, in 2D (middle row) and 3D (bottom row) format, of each of the three electrodes

### 4.2 Electrochemical test results

EIS was the first test for the EDLC cell and the results are presented in Fig.4(a), together with the values of characteristic resistances reported in the figure caption as determined from the Nyquist

for the EDLC cell of an area of 1.77 $cm^2$. Fig.4(a) is a Nyquist plot of the imaginary impedance, $Z_{im}$, versus the real impedance, $Z_{re}$, where:

$$-Z_{im} = -L_{cell}\omega + \frac{1}{\omega C_{cell}} \quad (15)$$

and also where $L_{cell}$ is the inductance, $C_{cell}$ is the capacitance and ω is the angular frequency, given as a function of frequency, f, by the relation: $\omega = 2\pi f$. The first intercept of the curve with $Z_{re}$ denotes resistance, $R_1$, which represents a combination of electrolyte, electrode and separator resistances. The $Z_{re}$ cord between the two intercepts of the curve with the $Z_{re}$ axis, $R_c$, represents the contact resistance between the electrode and current collector. The equivalent-in-series resistance, ESR, is then given by: $ESR = R_1 + R_c$.

Converting the resistance values for a cell area of 1 $cm^2$, to be able to compare against EDLCs with other electrolytes, the resistance values of the EDLC of this study with electrolyte 1M $LiPF_6$/EC:EMC are compared with those of the corresponding EDLCs with typical electrolyte 1M $TEABF_4$ in acetonitrile or PC in Table 1. It is obvious that the low viscosity acetonitrile solvent yields an electrolyte with the lowest resistance as a total ESR value and its components $R_1$ and $R_c$. On the other hand, the electrolyte 1M $LiPF_6$/EC:EMC of this study raises both resistance components and the total ESR value compared to $TEABF_4$ in both acetonitrile and PC, which may be attributed to the high viscosity of the solvent mixture EC:EMC 50:50 v/v, especially the very high viscosity of EC. At this stage it must be mentioned that whereas EDLC coin cells of 1.77 $cm^2$ were fabricated in this study, small EDLC pouch cells of rectangular shape 1x2 cm were fabricated in the experimental studies [7] and [33] and were tested under load. Hence, the cells in Table 1 were under different compression during testing in each case, so such differences might have had additional effects on resistance values.

**Table 1.** Key performance indicators from experimental data of EDLCs with different electrolyte but the same electrode coating and same current collector.

| **Electrolyte** | **$R_1$ (ohm cm$^2$)** | **$R_c$ (ohm cm$^2$)** | **ESR = $R_1$ + $R_c$ (ohm cm$^2$)** | **$C_{el,sp}$ (F g$^{-1}$)** |
|---|---|---|---|---|
| 1M $LiPF_6$/EC:EMC (this study) | 19.3 | 29.2 | 48.5 | 50.5 |
| 1.5 M $TEABF_4$/ acetonitrile [7] | 0.66 | 0 | 0.66 | 58.5 |
| 1 M $TEABF_4$/ PC [33] | 4.8 | 6.2 | 11 | 64 |

Fig.4(b) presents the results of the third cycle of CV tests at 1 mV s$^{-1}$ to different maximum voltage values. In general, as the end-voltage value is increased, the CV curve is observed to evolve to a bow shape, with an evident degradation peak for potential values above 3.3 V. Considering CVs up to a maximum voltage of 3 V, a mean electrode specific capacitance, $C_{el,sp}$ = 50.5 F g$^{-1}$, is determined from the midpoint of the full voltage range tested. This is the lowest capacitance value compared to the corresponding values related to the other two typical EDLC electrolytes, as displayed in Table 1, in which $TEABF_4$/PC exhibits the highest specific capacitance due to the large dielectric constant of PC.

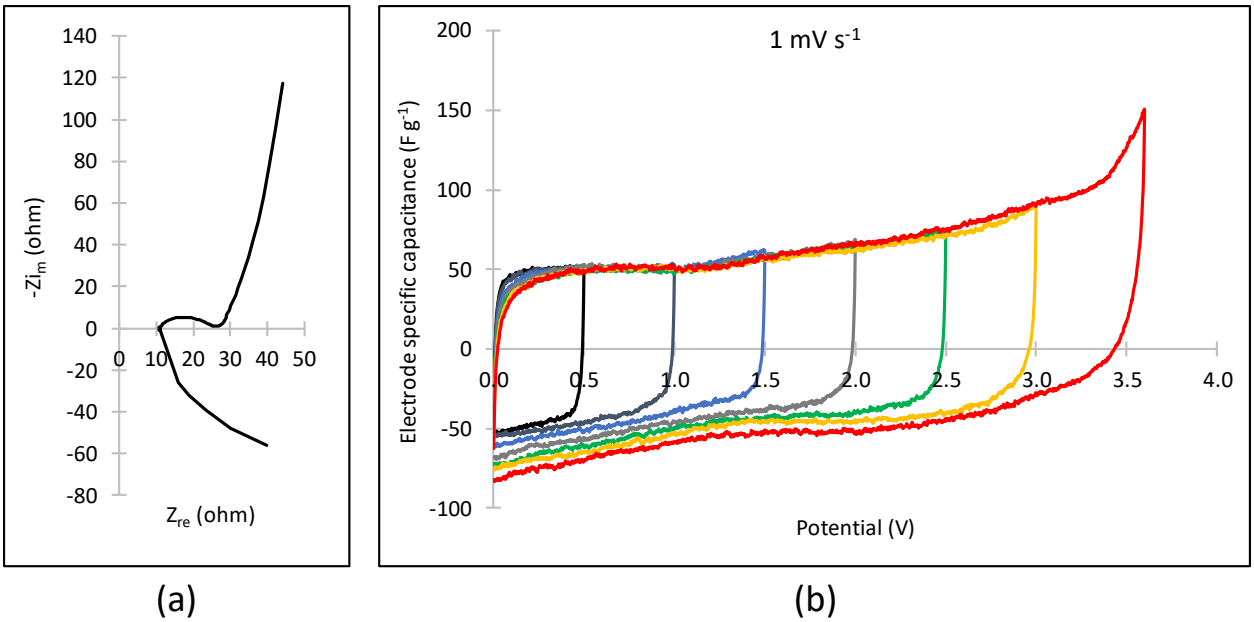


**Fig.4** Test data for the EDLC cell: (a) Nyquist plot: electrolyte, coating, separator resistance, $R_1$ = 10.9 ohm, contact resistance with current collectors, $R_c$= 16.5 ohm, equivalent in series resistance, ESR=27.4 ohm; (b) CV tests at 1 mV $s^{-1}$ to different maximum voltage values

Fig.5(a) presents the GCD data at different currents from the third GCD cycle at each current. GCD tests were carried out to a maximum voltage of 3 V. Energy and power densities were determined from the discharge phase of each GCD set of data in Fig.5(a), with respect to the total mass of the two electrodes, and are presented in a Ragone plot in Fig.5(b). The maximum energy density of 13.7 Wh/$kg_{els}$ and maximum power density of 1.3 kW $kg_{els}$ may be compared with those of the equivalent EDLC with electrolyte 1M $TEABF_4$ in acetonitrile, 18.8 Wh/$kg_{els}$ and 16.2 kW $kg_{els}$ [7]: as expected, the low conductivity of the Li-ion electrolyte of this study, due to the high viscosity of the solvent mixture EC:ECM 50:50 v/v, lowers to a very large extent the EDLC power

density and has also an effect on lowering its energy density, compared to the EDLC with the low viscosity electrolyte solvent acetonitrile.

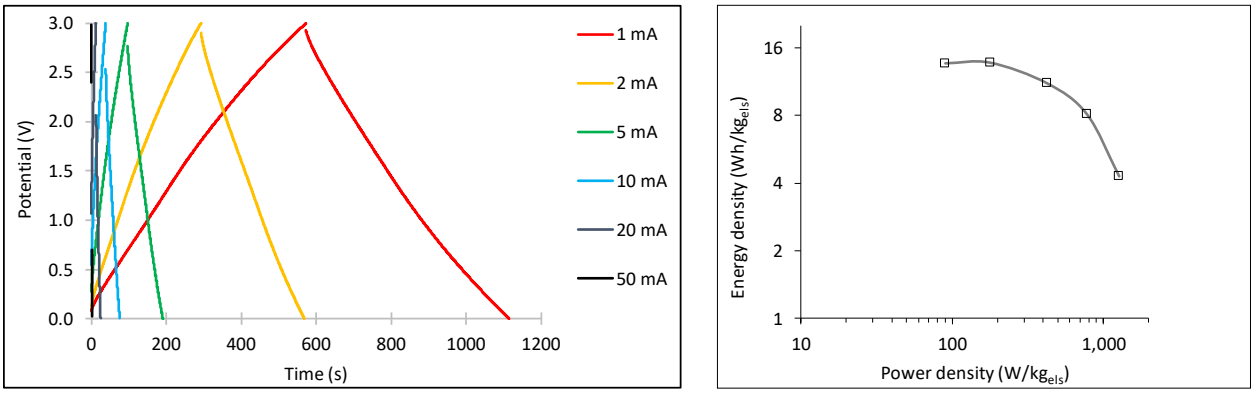


(a) (b)

**Fig.5** Test data for the EDLC cell: (a) GCD data at different currents (b) Ragone plot from the discharge data of GCD tests, energy and power density values with respect to the mass of the two electrodes

## 5. COMPUTER SIMULATIONS

### 5.1 Electrolyte

Table SI-1 presents the simulation input data related to the electrolyte 1M $LiPF_6$/EC:EMC 50:50 v/v. The solvated ion sizes were determined on the basis of the results of molecular dynamics (MD) simulations by Ong et al [34] from which the coordination numbers were determined for the solvated ions $Li^+$ and $PF_6^+$, in dissociated state; the solvated ions in their minimized state were then visualized in Materials Studio 6.1, in the form of their van der Waals volumes: their maximum and minimum dimensions were measured and are presented in Table SI-1. It has also been reported

that $PF_6^-$ is weakly solvated [34], hence, upon desolvation in Table SI-1 it loses all 3 coordinated solvent molecules.

On the other hand, $Li^+$ has a high desolvation energy barrier. Minimum energy simulations of a $Li^+$ ion solvated with 4 EC:EMC molecules altogether (it has a coordination number of 4 for EC:EMC [34]) between two graphene sheets result in a deformed solvated ion, maintaining all its solvent molecules (see Fig.6), where the initial tetrahedral shape of the free solvated ion [34] has been deformed to a "flat shape" between the graphene sheets, the latter also bulging to accommodate the "flat" solvated $Li^+$ ion. For this reason, small slit-shaped micropores are accessible by "flat" solvated $Li^+$ ions, of coordination number of 4, without any proper desolvation given also the high value of their desolvation energy. Pores of size equal to or larger than $d_{Li+/EC:EMC}$ = 1.8 nm can accommodate the full 3d tetrahedral solvated $Li^+$ ions.

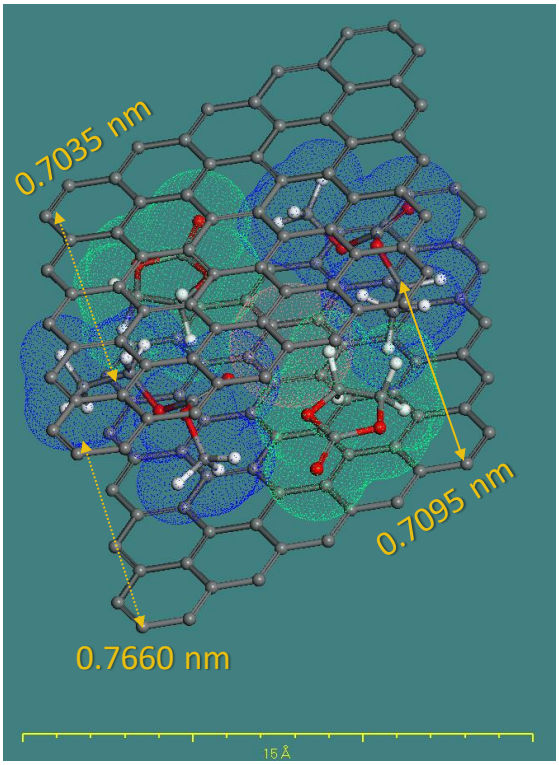

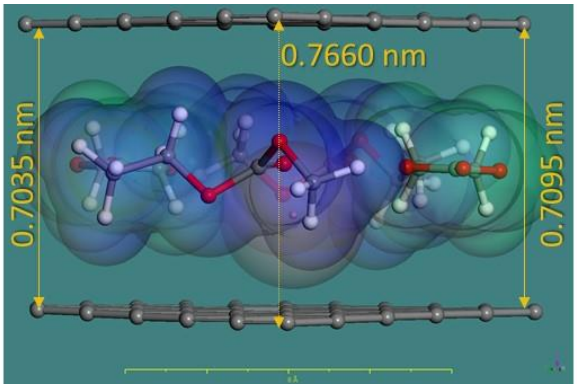


**Fig.6** A $Li^+$ ion coordinated with 2 EC and 2 EMC molecules, between two graphene sheets, at its minimum energy (visualisation of van der Waals volumes in Materials Studio 6.1)

### 5.2 Results of the continuum model simulations

The first simulation case study matches the conditions for the GCD tests for the EDLC coin cell with *Electrode 1* and electrolyte 1M $LiPF_6$/EC:EMC 50:50 v/v. The input data include a cell area of 1.77 $cm^2$ and electrode coating areal density of 4.6 mg $cm^{-2}$, according to the experimental details presented in section 3.2 and the discrete PSD of *Electrode 1* in Fig.2. Fig.7(a) presents the predicted GCD results and their comparison with the corresponding experimental data: In general, there is good comparison between predictions and experimental data, with some differences for the low current 2 mA curve. However, the average electrode specific capacitance determined from the first (after the voltage drop) and last point of each discharge curve, assuming linearity, exhibits good agreement between the predictions and the experiment at the low currents of 2-10 mA, as shown in Fig.7(b). For the currents of 20 and 50 mA, the experimental capacitance values are lower than the predicted values. It seems that the predicted ion transport at high currents is better than the real ion transport, which exhibits very high ESR as also seen in Table 1 for the Li-ion electrolyte compared to typical EDLC electrolytes $TEABF_4$ in acetonitrile or PC: poor ion

transport at high currents means that ions do not reach micropores to charge their surface and, hence, fail to reach the maximum available pore capacitance that is achieved at low currents.

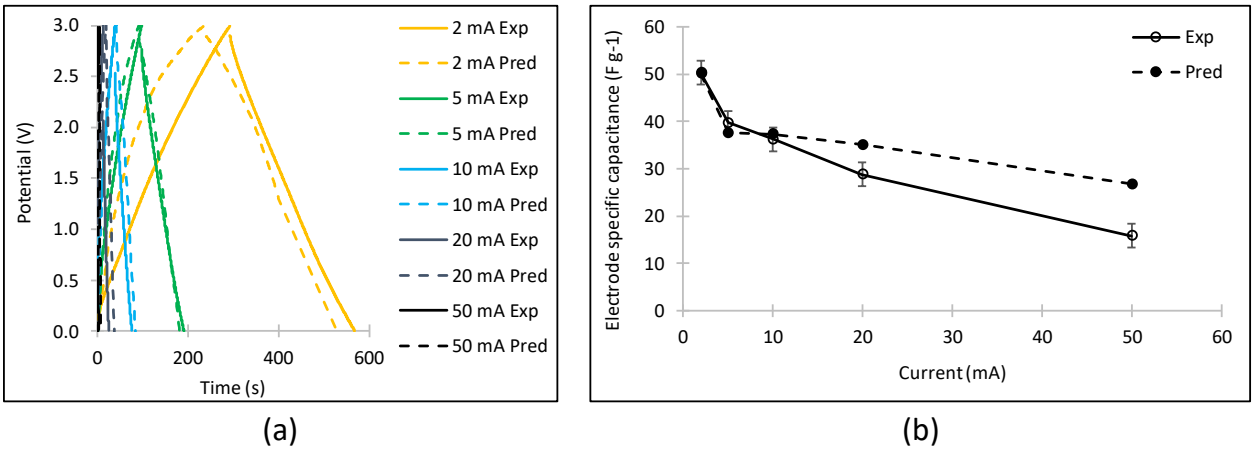


**Fig.7** Case study of GCD tests of the EDLC coin cell with *Electrode 1* and electrolyte 1M $LiPF_6$/EC:EMC 50:50 v/v: a comparison between the simulation predictions and the experimental data at different currents: (a) GCD curves; (b) electrode specific capacitance from the discharge curves of Fig.6(a)

In an effort to elucidate the reasons behind the difference in the shape of the GCD curves between the experimental and simulation results at the low current in Fig.7, the predicted ion concentration profiles as they evolve with time during charge and discharge are presented in Fig.8. First of all, the predicted duration of the charge phase (0 to 3 V) and discharge phase (3 to 0 V) was noted as 234 s and 296 s, respectively, from the simulation predictions of Fig.7, against the corresponding experimental data of 293 s for charge and 275 s for discharge.

Fig.8 displays almost linear decrease in concentration of $Li^+$ in cathode during charge (234 s) to a minimum concentration of 0.7 M, and symmetric linear increase in discharge (233 s) back to the original electrolyte concentration of 1 M. The maximum decrease in $Li^+$ concentration in charge

occurs in 1.4 nm, 1.6 nm and 1.77 nm pores, which is in fact the right-hand-side peak (1.4 nm) and the two consecutive points in the discrete PSD data of *Electrode 1* in Fig.2. The $Li^+$ ions move to the anode during charge, where the $Li^+$ concentration increases approximately linearly to a maximum at 235 s of charge, and decreases also linearly in discharge to the original electrolyte concentration of 1 M after 234 s of discharge for almost all pore sizes, apart from the 119 nm macropore in which the $Li^+$ concentration returns to 1 M after 296 s. The maximum $Li^+$ concentration increase in the anode during charge, to 1.3 M, also occurs in the 1.4 nm, 1.6 nm and 1.77 nm pores, all of which are just below the size of a tetrahedral solvated $Li^+$ ion $d_{Li+/EC:EMC}$ = 1.8 nm (Table SI-1), in which the code considers $Li^+$ ion transport in the form of a flat solvated ion of thickness $d_{Li+}$ = 0.56 nm, which can move easily in such pore sizes.

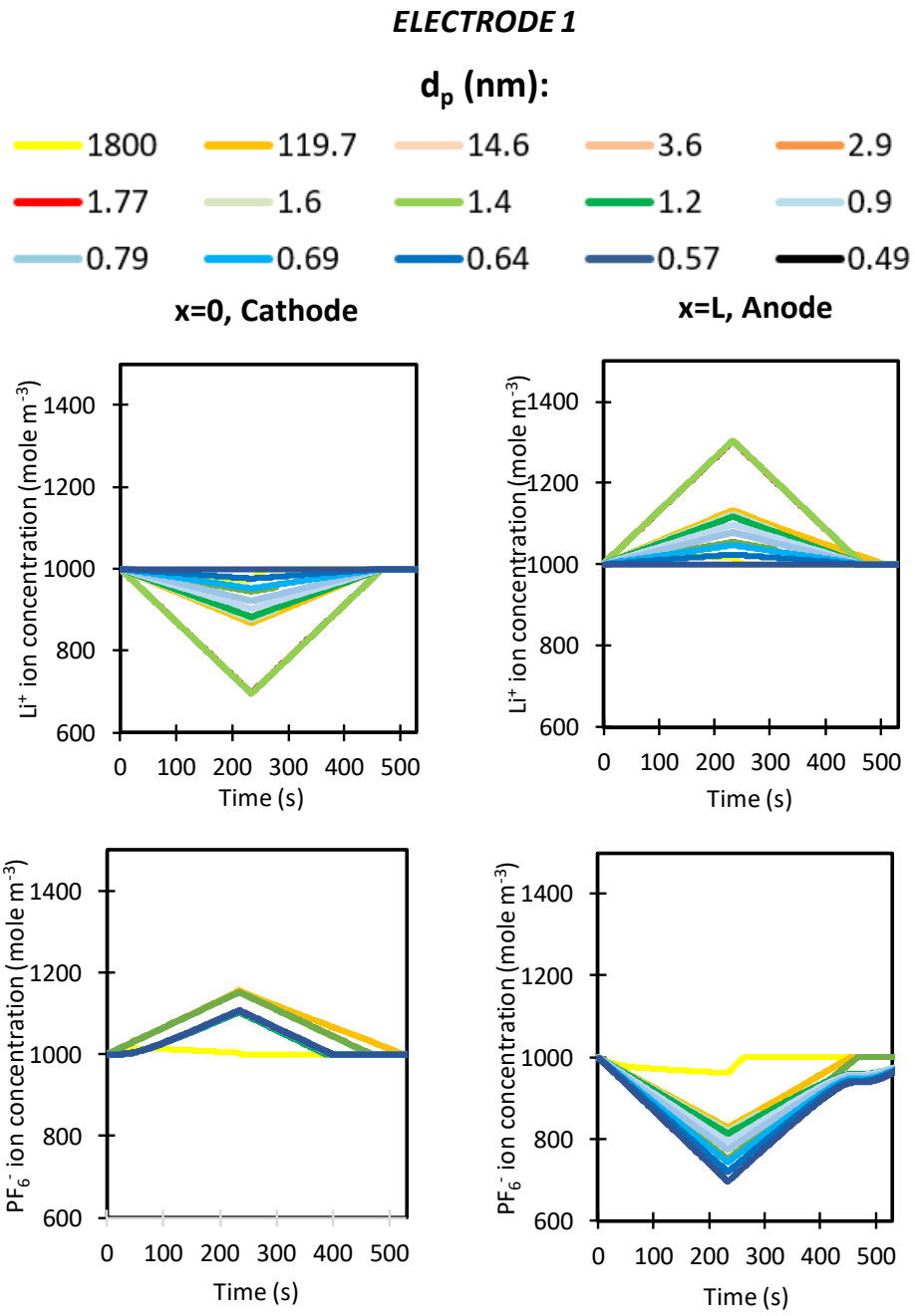


**Fig.8** Predicted ion concentration profiles against time at x=0 (cathode/current collector) and x=L (anode/current collector) for EDLC with *Electrode 1* and 1 M $LiPF_6$/EC:EMC electrolyte in GCD simulation at 2 mA

Looking at the $PF_6^-$ anion profiles, the $PF_6^-$ concentration rises in the cathode during charge to a maximum of 1.15 M and decreases during discharge, which considered in association with the $Li^+$ ion profiles in the cathode demonstrates a mechanism of ion exchange in the cathode during both charge and discharge. All the $PF_6^-$ concentration profiles take about 235 s to rise to their maximum concentration at the end of charge. The $PF_6^-$ concentration profile in the 119 nm pore is the slowest to return to 1 M concentration at 295 s of discharge. The maximum concentration of 1.15 M at the end of charge has been reached in the meso- and macropores of 2.9 nm, 3.6 nm, 14.6 nm and 119 nm; amongst these pore sizes, the $PF_6^-$ concentration profile in the 2.9 nm, 3.6 nm and 14.6 nm returns to 1 M at 230 s of discharge (similar to the charge time). $PF_6^-$ ion transport seems slow in pores lower than 1.8 nm (which is in fact the limit of the tetrahedral solvated $Li^+$ ion), where there is a lag of about 60 s for the $PF_6^-$ concentration to rise at the beginning of charge, the maximum concentration at the end of charge is 1.1 M, and then the $PF_6^-$ concentration falls symmetrically in discharge to 1 M at 163 s. With regards to the anode, the $PF_6^-$ concentration falls to a minimum of 0.7 M at 238 s at the end of charge and rises back to 1 M at 231 s of discharge for the meso- and macropores, larger than 1.8 nm. However, in pores smaller than 1.2 nm, the $PF_6^-$ concentration takes long time to increase to 1 M at the end of discharge with a lag after 231 s of discharge, delaying the end of discharge to 292 s. The reason for this is that towards the end of discharge there is not sufficient amount of electrochemical energy, $E_{EC}$, to overcome the desolvation energy barrier and, hence, the decay factor, $F_{decay}$, becomes significant and delays the $PF_6^-$ ion transport entering small micropores. We believe that this has a chain effect in the last stage of discharge, felt by the macropore of 119 nm, in delaying to empty the cathode macropore of 119 nm from $PF_6^-$ ions intended to move to the anode micropores, as well as delaying emptying the anode macropore of 119 nm of $Li^+$ ions.

Furthermore, computer simulations using the continuum model have been carried out and are presented to assess carbonaceous electrode materials with different PSDs, more specifically the PSDs presented in Fig.2 for *Electrode 2* and *Electrode 3*, which in fact have been determined from real experimental materials: TE320 AC-based coating and AC Kynol fabric ACC-507-15, respectively, as presented in section 3.1. Fig.9 presents the predictions for GCD tests at different currents and the GCD curves for EDLCs with different electrode materials: *Electrode 1*, *Electrode 2* and *Electrode 3*, of different PSDs while all the rest of input data (electrolyte, cell area and electrode areal density) are the same. It can be seen that the PSDs of *Electrode 2* and *Electrode 3* offer lower capacitance than *Electrode 1*. This is most interesting, as *Electrode 3*'s PSD was optimised for high energy density EDLCs with 1.5 M $TEABF_4$/acetonitrile electrolyte [1] but it exhibits lower energy density than *Electrode 1* for the Li-ion electrolyte of this study.

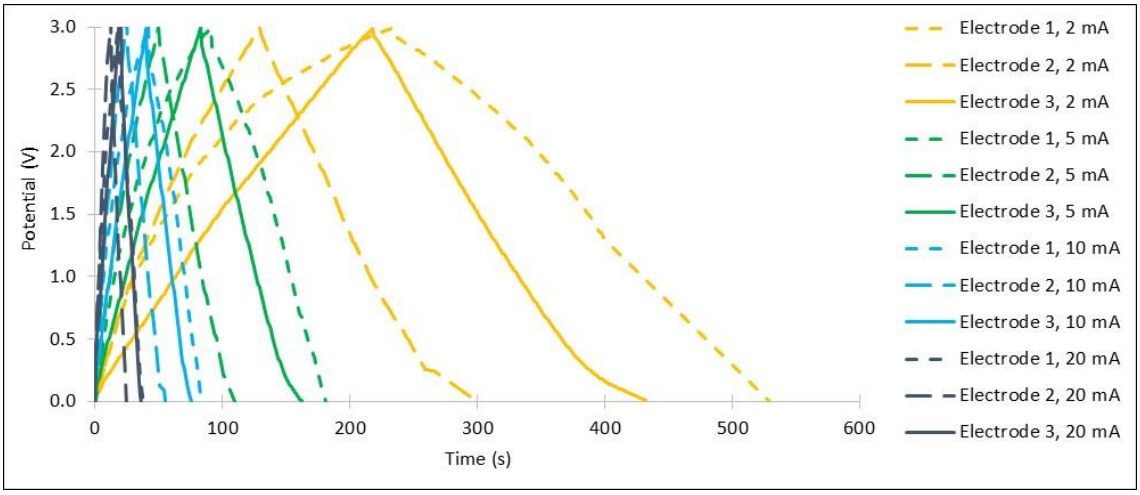


**Fig.9** Simulation case studies of GCD tests of the EDLC coin cell with electrolyte 1M $LiPF_6$/EC:EMC 50:50 v/v and different electrode materials: *Electrode 1*, *Electrode 2* and *Electrode 3*: predictions at different currents

The shape of the discharge curves for *Electrode 2* and *Electrode 3* is different from the shape of *Electrode 1*, with the former two exhibiting a deceleration of discharge towards the end. The predicted ion concentration profiles for *Electrode 2* in Fig.10 exhibit smaller concentration changes at the end of charge than those for *Electrode 1* in Fig.8. This is attributed to the lack of macro- and mesopores (119 nm and 14.6 nm) in the discrete PSD of *Electrode 2* compared to *Electrode 1* which slows down ion transport to micropores, and also to the small specific volume of micropores below 1 nm for *Electrode 2* compared to *Electrode 1* which would effectively reduce the specific capacitance of *Electrode 2* with regards to the "flat" solvated $Li^+$ ions and desolvated $PF_6^-$ ions. The total GCD time for *Electrode 3* is between those for *Electrode 1* and *Electrode 2*, which can be attributed to some meso- and macropores being present in *Electrode 3* but not at as high specific volume as for *Electrode 1*.

The ion concentration profiles in Fig.,10 and 11 against Fig.8 display similar trends of ion exchange during charge and discharge in cathode and anode and delay effects for the discharge due to delays in the desolvation of $PF_6^-$ ions. Especially for *Electrode 2* in Fig.10, the effect of delay in $PF_6^-$ ion desolvation is evident at the beginning of charge in the cathode, 19 s delay for 1.3 nm pores (with follow on effect of sharper concentration rise in 1.6 nm pores in first 19 s of charge due to ion accumulation in the pore size immediately upstream the 1.3 nm pores) and 56 s delay for micropores smaller than 1.3 nm; symmetric charge-discharge profiles are observed for most concentration profiles, apart for a total discharge time delayed to 300 s for returning to these micropores towards the end of discharge. This delay of $PF_6^-$ ion desolvation is the main factor causing the change in slope to slower ion transport towards the end of discharge at low GCD currents in Fig.9 for both *Electrode 2* and *Electrode 3*.

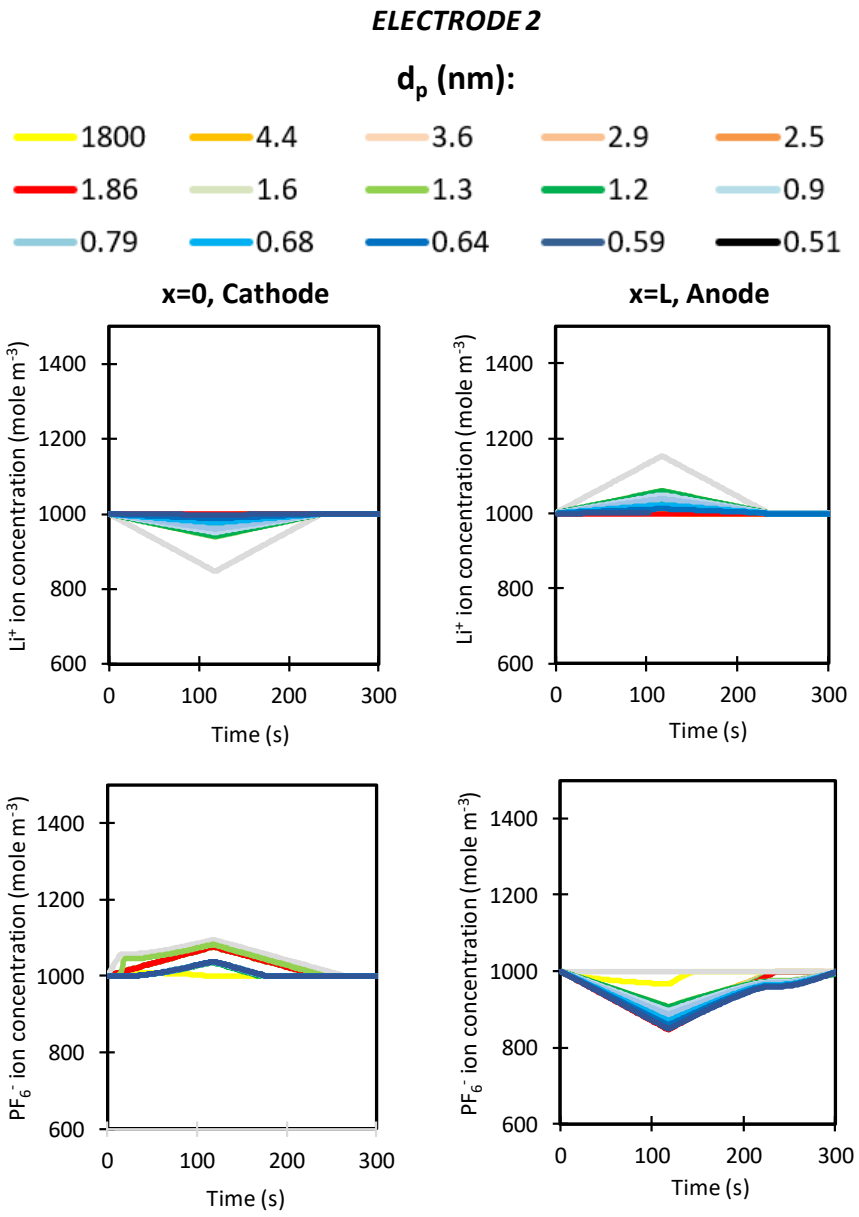


**Fig.10** Predicted ion concentration profiles against time at x=0 (cathode/current collector) and x=L (anode/current collector) for EDLC with *Electrode2* and 1 M $LiPF_6$/EC:EMC electrolyte in GCD simulation at 2 mA

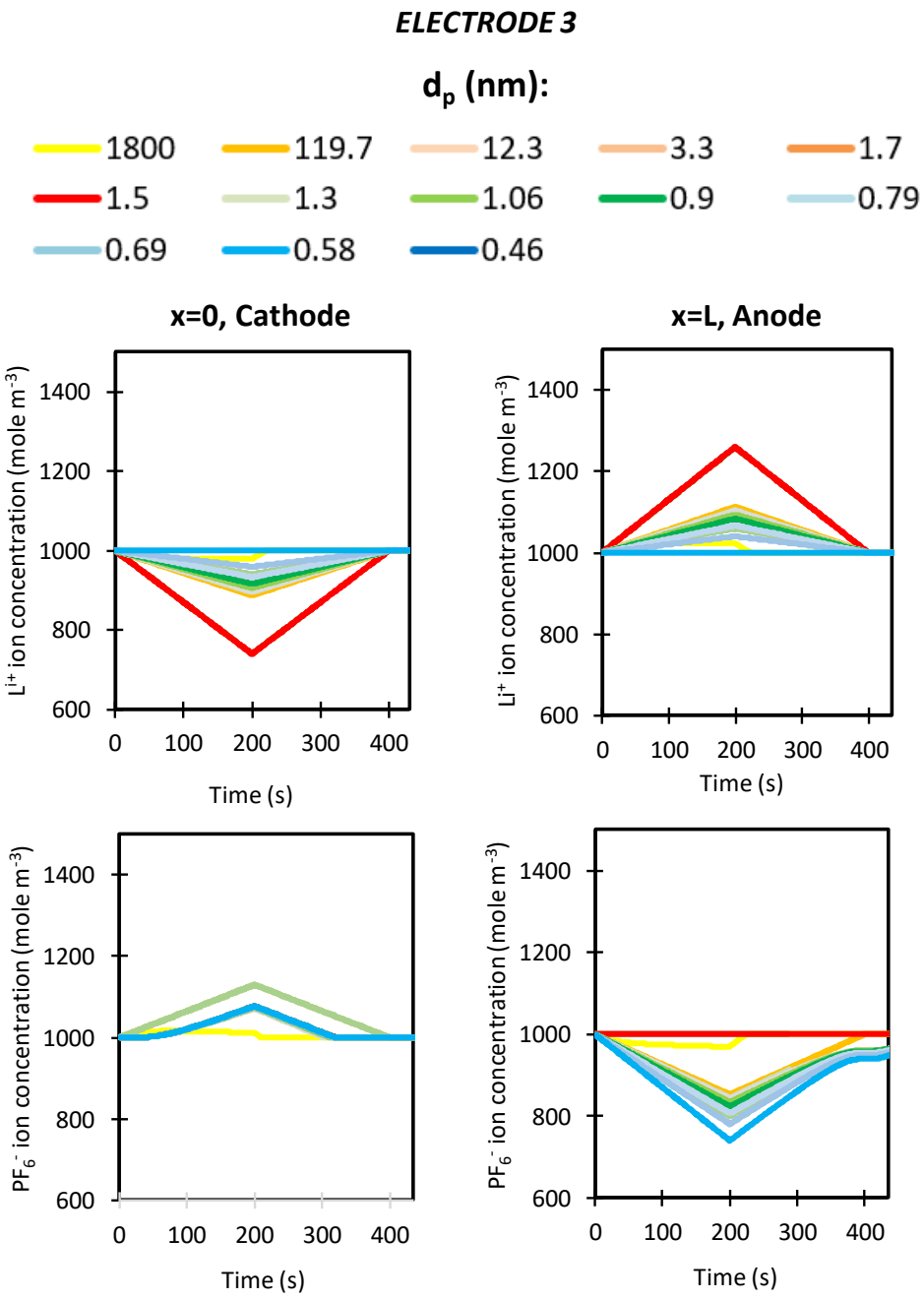


**Fig.11** Predicted ion concentration profiles against time at x=0 (cathode/current collector) and x=L (anode/current collector) for EDLC with *Electrode3* and 1 M $LiPF_6$/EC:EMC electrolyte in GCD simulation at 2 mA

## 6. CONCLUSION

The present study has investigated EDLCs with a lithium-ion electrolyte and AC electrodes. The AC electrode materials in two-electrode symmetric EDLC cells with electrolyte 1 M $LiPF_6$ in EC:EMC 50:50 v/v were shown to have similar stable potential window of 0-3 V as in typical EDLC electrolyte $TEABF_4$ in acetonitrile or PC. However, due to the higher viscosity of the tested electrolyte 1 M $LiPF_6$ in EC:EMC 50:50 v/v compared to electrolytes in acetonitrile or PC, a symmetric EDLC with *Electrode 1* materials exhibited higher ESR, lowering mainly the power density to 1.3 kW $kg_{els}$ which also lowers the energy density to a lesser extent, 13.7 Wh/$kg_{els}$, compared to 16.2 kW $kg_{els}$ and 18.8 Wh/$kg_{els}$, respectively, for an equivalent EDLC with electrolyte 1.5 M $TEABF_4$ in acetonitrile from past studies within our group [7].

Three AC electrode materials of different PSD and specific pore surface area, BET = 808.3 $m^2 g^{-1}$, 1273.7 $m^2 g^{-1}$ and 1491 $m^2 g^{-1}$ for *Electrode 1*, *Electrode 2* and *Electrode 3*, respectively, were assessed for a symmetric EDLC with electrolyte 1 M $LiPF_6$ in EC:EMC 50:50 v/v. Amongst these three AC electrode materials, *Electrode 2* had a broad peak in the range of 0.5-3 nm and *Electrode 1* and *Electrode 3* had binomial PSDs, with *Electrode 1* having an increasing cumulative specific pore volume (after the initial fast rise for pore sizes in the range of 0.5 to 3.6 nm) all the way to the final measured pore size of 180 nm. On the other hand, *Electrode 2* and *Electrode 3* had almost flat cumulative specific pore volume lines for pores greater than 2.9 nm and 3.3 nm, respectively.

The assessment of the electrode materials was carried out via computer simulations based on a continuum ion and charge transport model with volume-averaged equations, considering the full discretised pore size distribution for each electrode material. The model considered transport of

$Li^+$ ions in solvated state, with "flat" solvated $Li^+$ ions in micropores smaller than 1.8 nm and tetrahedral solvated $Li^+$ ions in larger pores. $PF_6^-$ ions were desolvated in micropores smaller than 1.4 nm and solvated in larger pores. A decay factor was incorporated for the transport of desolvated ions, due to the energy barrier needed to overcome for their desolvation.

The computer simulations revealed a mechanism of ion exchange in both cathode and anode during the simulated GCD tests at different currents. The delay in the desolvation of $PF_6^-$ ions led to delays in the rise of $PF_6^-$ concentration in small micropores in the cathode during charge and in the return of $PF_6^-$ ions to small micropores in the anode during discharge, affecting the overall shape of the GCD curves and slowing down the discharge GCD curve towards the last stage of discharge.

The computer simulations concluded that *Electrode 2* held the lowest stored charge and had the shortest GCD duration (total time and in each phase: charge or discharge) compared to the other two electrode materials in EDLCs with the same electrolyte 1M $LiPF_6$ in EC:EMC 50:50 v/v; *Electrode 2* is based on TE320 AC coating which, it must be noted, was optimised in the past specifically for EDLCs with electrolyte 1.5 M $TEABF_4$ in acetonitrile [1]. The simulation results concluded that *Electrode 1* was the best of the three electrode materials in relation to the electrolyte 1M $LiPF_6$ in EC:EMC 50:50 v/v, and is in fact the electrode material used in the present experimental study.

Overall, the present study has demonstrated the importance of designing porous electrode materials in EDLCs with not only high specific surface area, but most importantly with a PSD with macro, meso- and large micropores accommodating the solvated ions of the electrolyte and small

micropores still accessible by the desolvated ions. The continuum ion and charge transport model, incorporating the pore size distribution and solvated and desolvated ions, has also been proven a most valuable tool in the design of porous electrode materials.

## ACKNOWLEDGEMENTS

The University of Surrey authors gratefully acknowledge funding of this study by EPSRC under the HiPoBat project: ISCF Wave 1: High Power Material Hybridised Battery, EP/R022852/1.

## REFERENCES

[1] R.Fields, C.Lei, F.Markoulidis, C.Lekakou, The Composite supercapacitor, Energy Technology 4 (2016) 517–525.
[2] W. Zuo, R. Li, C. Zhou, Y. Li, J. Xia, J. Liu, Battery-supercapacitor hybrid devices: recent progress and future prospects, Adv. Sci. 4 (2017) 1600539.
[3] C. Lei, N. Amini, F. Markoulidis, P. Wilson, S. Tennison, C. Lekakou, Activated carbon from phenolic resin with controlled mesoporosity for an electric double-layer capacitor (EDLC), Journal of Materials Chemistry A 1 (2013) 6037-6042.
[4] E.C.Vermisoglou, T.Giannakopoulou, G.E.Romanos, N.Boukos, M.Giannouri, C.Lei, et al, Non-activated high surface area expanded graphite oxide for supercapacitors, Applied Surface Science, Part A 358 (2015) 110-121.
[5] E.C. Vermisoglou, T. Giannakopoulou, G. Romanos, M. Giannouri, N. Boukos, C. Lei, et al, Effect of hydrothermal reaction time and alkaline conditions on the electrochemical properties of reduced graphene oxide, Applied Surface Science, Part A 358 (2015) 100-109.
[6] F.Markoulidis, C.Lei, C.Lekakou, Investigations of activated carbon fabric-based supercapacitors with different interlayers via experiments and modelling of electrochemical processes of different timescales, Electrochimica Acta 249 (2017) 122-134.
[7] F.Markoulidis, C.Lei, C. Lekakou, D.Duff, S.Khalil, B.Martorana, et al, A method to increase the energy density of supercapacitor cells by the addition of multiwall carbon nanotubes into activated carbon electrodes, Carbon 68 (2014) 58–66.
[8] C. Lei, C.Lekakou, Activated carbon–carbon nanotube nanocomposite coatings for supercapacitor application, Surface and Coatings Technology 232 (2013) 326-330.
[9] C. Zhao, W. Zheng, A review for aqueous electrochemical supercapacitors, Front. Energy Res. (2015) https://doi.org/10.3389/fenrg.2015.00023

[10] R. Lin, P.L. Taberna, J. Chmiola, D. Guay, Y. Gogotsi, P. Simon, Microelectrode study of pore size, ion size, and solvent effects on the charge/discharge behavior of microporous carbons for electrical double-layer capacitors. Journal of The Electrochemical Society 156 (2009) A7-A12.

[11] J. Huang, B.G. Sumpter, V. Meunier, Theoretical model for nanoporous carbon supercapacitors, Angew. Chem. Int. Ed. 47 (2008) 520 –524.

[12] J. Bates, Modelling and simulations of energy storage devices. PhD Thesis, University of Surrey, UK (2020).

[13] L.Yu, G.Z. Chen, Ionic liquid-based electrolytes for supercapacitor and supercapattery, Front. Chem. (2019) https://doi.org/10.3389/fchem.2019.00272.

[14] C.Lekakou, O.Moudam, F.Markoulidis, T.Andrews, J.F.Watts, G.T.Reed, Carbon-based fibrous EDLC capacitors and supercapacitors, Journal of Nanotechnology (2011) 409382, doi: 10.1155/2011/409382C.

[15] E.C. Vermisoglou, M. Giannouri, N. Todorova, T. Giannakopoulou, C. Lekakou, C. Trapalis, Recycling of typical supercapacitor materials, Waste Management & Research 34 (2016) 337–344.

[16] E.M.Kampouris, C.D.Papaspyrides, C.N.Lekakou, A model process for the solvent recycling of polystyrene, Polymer Engineering and Science 28(1988) 534-537.

[17] E.M.Kampouris, C.D.Papaspyrides, C.N.Lekakou, A model recovery process for scrap polystyrene foam by means of solvent systems, Conservation & Recycling 10(1987) 315-319.

[18] A.K.Murugesh, A.Uthayanan, C.Lekakou, Electrophoresis and orientation of multiple wall carbon nanotubes in polymer solution, Applied Physics A: Materials Science and Processing 100 (2010) 135-144.

[19] T. Zhang, B. Fuchs, M. Secchiaroli, M. Wohlfahrt-Mehrens, S. Dsoke, Electrochemical behavior and stability of a commercial activated carbon in various organic electrolyte combinations containing Li-salts, Electrochimica Acta 218 ( 2016) 163-173.

[20] S.A. Krachkovskiy, A.D. Pauric, I.C. Halalay, G.R. Goward, Slice-selective NMR diffusion measurements: a robust and reliable tool for in situ characterization of ion-transport properties in lithium-ion battery electrolytes, J. Phys. Chem. Lett. 4 (2013) 3940-3944.

[21] W.Lai, F.Ciucci, Mathematical modeling of porous battery electrodes—Revisit of Newman's model, Electrochimica Acta 56 (2011) 4369-4377.

[22] P.M. Biesheuvel, Y. Fu, M.Z. Bazant, Diffuse charge and Faradaic reactions in porous electrodes, Phys. Rev. E 83 (2011) 061507, 1-17.

[23] A.D.Gosman, C.Lekakou, S. Politis, R.I.Issa, M.K.Looney, Multidimensional modelling of turbulent two-phase flows in stirred vessels, AIChE J. 38 (1992) 1946-1956.

[24] S.Amico, C.Lekakou, Flow through a two-scale porosity, oriented fibre porous medium, Transport in Porous Media 54 (2004) 35-53.

[25] C.Lekakou, S.Edwards, G.Bell, S.C.Amico, Computer modelling for the prediction of the in-plane permeability of non-crimp stitch bonded fabrics, Composites A: Applied Science and Manufacturing 37 (2006) 820-825.

[26] Y. Elsayed, C. Lekakou, P. Tomlins, Modeling, simulations and optimization of smooth muscle cell tissue engineering for the production of vascular grafts, Biotechnology and Bioengineering 116 (2019) 1509-1522.

[27] S. Sahu and M.Zwolak, Colloquium: Ionic phenomena in nanoscale pores through 2D materials, Rev. Mod. Phys. 91 (2019) 021004.
[28] D. A. G. Bruggeman, Berechnung verschiedener physikalischer Konstanten von heterogenen Substanzen. I. Dielektrizit¨atskonstanten und Leitf¨ahigkeiten der Mischkorper aus isotropen Substanzen, Ann. Phys. 416 (1935) 636-664.
[29] U. Sahapatsombut, H. Cheng, K. Scott, Modelling of operation of a lithium-air battery with ambient air and oxygen-selective membrane, Journal of Power Sources 249 (2014) 418-430.
[30] R.E. Beck, J.S. Schultz, Hindered diffusion in microporous membranes with known pore geometry, Science 170 (1970) 1302-1305.
[31] G.E. Murch, The exact Nernst-Einstein equations and the interpretation of cross phenomenological coefficients in unary, binary, and ambipolar systems, Radiation Effects 73 (1983) 299-305.
[32] C.N.Lekakou, S.M.Richardson, Simulation of reacting flow during filling in reaction injection molding (RIM), Polymer Engineering Science 26 (1986) 1264-1275.
[33] C. Lei, P.Wilson, C.Lekakou, Effect of poly(3,4-ethylenedioxythiophene) (PEDOT) in carbon-based composite electrodes for electrochemical supercapacitors, J. Power Sources 196 (2011) 7823-7827.
[34] M.T. Ong,_O. Verners, E.W. Draeger, A.C.T. van Duin, V. Lordi, J.E. Pask, Lithium ion solvation and diffusion in bulk organic electrolytes from first principles and classical reactive molecular dynamics, Phys. Chem. B 119(2015) 1535-1545.